# Understanding the Parameters Affecting the Photoluminescence of Silicon Nanoparticles

Manuel J. Llansola Portolés,[†] Reinaldo Pis Diez,[‡] María L. Dell'Arciprete,[†] Paula Caregnato,[†] Juan José Romero,[†] Daniel O. Mártire,[†] Omar Azzaroni,[†] Marcelo Ceolín,[†] and Mónica C. Gonzalez*,[†]

[†]INIFTA, Departamento de Química, Facultad de Ciencias Exactas UNLP and [‡]CEQUINOR, Facultad de Ciencias Exactas, Universidad Nacional de La Plata, CC 962, 1900 - La Plata, Argentina

Ⓢ *Supporting Information*

ABSTRACT: Silicon nanoparticles of 1−5 nm size (SiNPs) were synthesized by a bottom-up (BU) approach involving a chemical wet method. The contribution of different emitters to the overall excitation−emission matrix was analyzed on the assumption that pure substances existing in a unique form show an excitation wavelength-invariant emission spectrum. The occurrence of emitters differing in size and aggregation was supported by transmission electron microscopy (TEM), small-angle X-ray scattering (SAXS), time-resolved single photon counting, and time-resolved anisotropy experiments. The effect on photoluminescence (PL) of the particle surface oxidation as a result of aging is studied and compared to that of surface oxidized particles obtained by a top-down (TD) approach following an electrochemical method with HF etching. Surface oxidation to SiO_x seems to introduce two different effects on the SiNP PL. An emission originated in surface states associated to

SiO_x was identified and observed for SiNPs synthesized by both BU and TD approaches. Blue-shifted excitation−emission spectra associated to a silicon core in embedded SiO_x nanostructures were also identified. Theoretical studies were carried out to help understand the observed results.
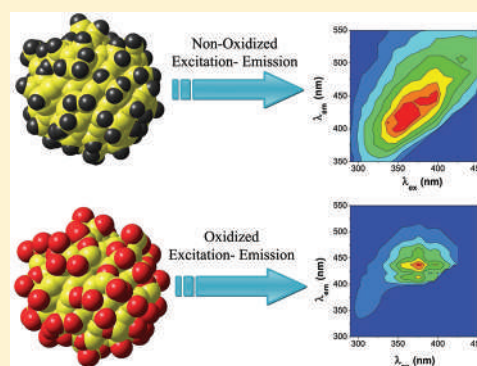
Silicon nanoparticles of 1−5 nm size (SiNPs) received great attention, as they combine size-dependent photoluminescence (PL) with the richness of silicon surface chemistry.[1] The momentum requirements which make bulk Si a rather inefficient light emitter are relaxed in the 1−5 nm size silicon crystals as a result of quantum confinement effects.[2] The optical emission properties of these chromophores can be tailored by suitably adjusting the height and width of the potential that confines electrons and holes. In spherically shaped colloidal dots, the band gap and oscillator strength can be tuned by variation of the diameter.[3] Silicon in the form of small structures shows a special interest because it is promising for light-emitting optoelectronics,[4] for photonics,[5] for light emitters in biological labeling,[6] and as photosensitizers of singlet oxygen.[7]

Silicon nanoparticles can be produced by comparatively simple methods. The synthesis procedures include electrochemical HF-mediated etching of crystalline Si wafers to yield porous silicon and further dispersion of the particles by ultrasound,[8] gas-phase synthesis,[9,10] and chemical reaction of Si precursors in solution.[11−14] However, significant differences are reported in the room-temperature PL of apparently similar particles obtained by different synthetic routes, as depicted in Table 1.

The wave functions of electrons and excitons in silicon nanoparticles of sizes smaller than the Bohr radius in bulk silicon (∼ 4.5 nm) are delocalized over the nanoparticle

Table 1. Average Particle Size and Emission Maximum for SiNPs Obtained by Different Synthetic Routes

synthesis procedure	average size/nm	$\lambda_{em}^{max}(\lambda_{exc})$/nm	surface coverage
anodic etched porous silicon[8]	1	320 (270) 380 (320)	H-capped or methyl ester-functionalized
argon/silane in a continuous flow atmospheric-pressure microdischarge reactor[10]	1.6	420 (360)	octyl-capped
$SiCl_4$ reduction in the presence of micelles[11,12]	1.6 ± 0.2	280−290 (260) shows peaking	alkyl-functionalized
$SiCl_4$ reduction in the presence of micelles[13]	1.8 ± 0.2	335 (290)	1-heptyl-capped
metathesis of sodium silicide with NH_4Br[14]	3.9 ± 1.3	438 (360−400)	octyl-capped

volume.[2,15] Therefore, the optical properties are sensitive not only to the size of the particles but also to the surface chemistry, network distortion, and geometry of the structures.[15] The difficulty in controlling these parameters during synthesis may introduce variability and contradiction within the results reported by different groups. The important role of surface reconstruction and composition in determining the PL

characteristics of the 1 nm particles is well described by theoretical studies which consider molecular-like energy levels.[16,17]

Surface oxidation is suggested to introduce defects, most likely located at the interface between the Si nanocrystals and the surrounding SiO_2 matrix.[18] These surface states were proposed to play an important role in the emission process.[19,20] The evidence in the literature indicates that while the excitation photons are absorbed by the Si semiconductor nanocrystal the emission may not be due mainly to electron−hole recombination as the nanocrystal morphological structure and the surrounding matrix optical properties also influence the luminescence process.[21] The relation between quantum confinement effects and surface states is suggested to determine the visible PL in nanocrystallites,[22] as reported for silicon nanoparticles of 1−1.5 nm size showing blue (3.0 eV) PL for H-terminated SiNPs and yellow-red emission (2.0 eV) after particle oxidation.[17] The latter effect due to the surface oxidation of the particles is opposite to that predicted by a quantum size model which considers that mainly the number of Si atoms in the core and the nanocrystal shape of the particle are responsible for the PL,[3] in agreement with the work reported by Hua on the oxidation of 5 nm particles.[9] The presence of oxygen in the particle structure is an evident reason for discrepancy as the origin and magnitude of these differences remain unclear. Since particle aging invariably leads to its oxidation, any technological use of the particles requires the understanding of its effect on the PL properties of SiNPs.

Herein we report the PL properties of SiNPs synthesized by a *bottom-up* (BU) approach and the effect on PL of surface oxidation to SiO_x as a result of particle aging. The PL of the BU-oxidized particles is compared to that of surface-oxidized particles obtained by a *top-down* (TD) approach. Theoretical calculations were carried out to support the discussion on the effects of surface SiO_x and network distortion on the particle PL.

■ MATERIALS AND METHODS

Materials. Toluene (99.7%, H_2O 0.005%), $SiCl_4$ (99%), ethyl ether (p.a. 99.9%), $LiAlH_4$ (95%), and tetraoctylammonium bromide (98%) were purchased from Sigma-Aldrich and employed without further purification. Deionized water (>18 MΩ cm, < 20 ppb of organic carbon) was obtained with a Millipore system. Argon (4 bands quality) and oxygen gas were both from La Oxígena S.A., Argentina.

SiNP Synthesis. Silicon nanoparticles were obtained in the laboratory by two different approaches. The BU-approach synthesis involved an adaptation of the $LiAlH_4$ reduction of $SiCl_4$ in the presence of tetraoctylammonium bromide (TOAB) reversed micelles reported by Rosso-Vasic.[11,13] Even after a tough purification workup, the samples remained partly contaminated with TOAB. The particles were allowed to age upon standing in an air-saturated toluene suspension in the dark for several weeks. Freshly prepared particles by BU synthesis are referred to as BUSiNP. On the other hand, the TD-approach involved an adaptation of the electrochemical method with HF etching of porous Si, which yields SiNPs covered by a SiO_x layer.[23] These particles are referred to as TDSiNP. See Supporting Information Particle Synthesis for details.

Equipment. *FT-IR spectra* were obtained with a Thermo Scientific Nicolet 380 FT-IR Spectrometer using KBr disks as

holders. Spectra were taken in the 4000−400 cm^{-1} range with 4 cm^{-1} resolution and corrected for the background signal.

The *attenuance spectra* were recorded with a double-beam Shimadzu UV-1800 spectrophotometer in a 1 cm quartz cuvette at a scan rate of 300 nm/min. The nanoparticle light scattering is calculated by fitting the 450−800 nm range attenuance to $a \times \lambda^{-4}$.[24] The corrected absorbance spectrum is obtained by subtraction of the scattering from the measured attenuance spectrum.

Room-temperature luminescence measurements were performed with a JOBIN-YVON SPEX FLUOROLOG FL3-11 spectrometer equipped with a Xe lamp as the excitation source, a monochromator for selecting the excitation and emission wavelengths (both with 1 nm bandpass gap), and a red sensitive R928 PM as detector. All spectra were corrected for the wavelength-dependent sensitivity of the detector and the source by recording reference data simultaneously. Additionally, emission spectra were corrected for Raman scattering by using the solvent emission spectrum. To estimate the emission quantum yield (Φ) of the synthesized Si nanoparticles,[25] PL emission spectra were collected at various excitation wavelengths. Identical measurements (excitation conditions, lamp energy, and spectrometer band-pass) were performed on 9,10-diphenylanthracene in cyclohexane, which emits between 400 and 500 nm with a known efficiency of 90% upon 275−405 nm excitation.[26]

Luminescence lifetime and anisotropy measurements were performed with a TCSPC (time-correlated single-photon counting) with LED excitation at 341 and 461 nm. Time-resolved emission spectroscopy (TRES) was performed, and results were fitted to an exponential model until optimal values of Chi square, residuals, and standard deviation parameters were attained. The emission spectrum associated with each lifetime may be obtained taking the contribution of each decay lifetime to the overall emission at a given wavelength, weighted by the emission intensity at the emission maximum.

Samples for transmission electron microscopy, TEM, were prepared by dipping a carbon-coated 300-mesh copper grid into a SiNP suspension in toluene and the solvent evaporated in air. TEM micrographs were taken with either a Phillips CM-10 or a JEOL 2010 F microscope. Images were analyzed employing the Image Tool 3.0 software (Health Science Center of the University of Texas, San Antonio, USA). Particle diameters were determined assuming that the particle area obtained from the TEM images is the projection of a spherical particle.

The X-ray photoelectron spectroscopy (XPS) spectra were obtained under UHV with a XR50 Specs GmbH spectrometer with Mg K(α) as the excitation source and a PHOIBOS 100 half sphere energy analyzer. Calibration was performed with Au 4f 7/2 (binding energy, BE, 84.00 eV) and with C 1s and N 1s internal standards with BE of 284.6 and 401.5 eV, respectively (see Supporting Information XPS spectra).

Small-angle X-ray scattering (SAXS) experiments were performed using the D02B-SAXS1 beamline of the Laboratorio Nacional de Luz Sincrotron (Campinas, Brazil). The sample-to-detector distance was set to 594 mm, and the working wavelength was 0.1608 nm. The sample temperature was kept at 22 °C using a circulating-water bath. Two parallel micas were used as windows defining an optical-path sample chamber of 1 mm. A CCD detector (MarCCD) was used to obtain 2D scattering patterns. SAXS data ($I(q)$ vs q, with the scattering vector $q = 4\pi \sin(\theta)/\lambda$, λ being the photon wavelength and θ

half the scattering angle) were obtained from azimuthal integration of the 2D scattering pattern. Corrections for parasitic scattering, dark signal, integrated current, and solvent signal were treated in the usual way. Data were analyzed using the low-q Guinier approximation or by obtaining their Pair Distance Distribution Function (PDDF) by means of indirect Fourier transformation methods implemented in the software GNOM 4.5.[27]

Bilinear Regression Analysis. A bilinear regression analysis taking advantage of the linearity of the emission wavelength with both the excitation wavelength and the factor reflecting the distribution of the probability of the various transitions from the lowest vibrational level of the first electronic excited level to the various vibrational levels of the ground state was applied to the experimental emission matrix. The analysis retrieves information on the minimum number of species and on their relative emission and absorption spectra. See Supporting Information Bilinear Regression Analysis for further details.

Modeling and Computational Methods. Geometry optimization of naked, H- and O-terminated SiNPs were carried out using the density functional tight binding (DFTB) method[28] with the aid of the DFTB+ program,[29,30] which allows SCC-DFTB calculations. Geometries are considered converged when the maximum element of the gradient vector of the energy with respect to nuclear coordinates is <0.01 au. The tolerance for charge self-consistency is fixed at 0.001 au.

Nanoparticles containing between 17 and 240 silicon atoms in their core were modeled as spherical portions of crystalline bulk silicon, in which the Si−Si bond length is 2.36 Å. Surface bond saturation with hydrogen and oxygen atoms was performed to study the importance of superficial oxidation in the surface stabilization and on the network disorder of nanoparticles. To this end, optimized silicon clusters, in vacuum and 0 K, were taken as the starting point, and all surface bonds were saturated with H atoms in one case and with O atoms in the other case.

SCC-DFTB optimized geometries are used to model excited states. The time-dependent density functional theory as implemented in the FIREFLY program[31] was used to obtain the band gaps. The hybrid GGA exchange and correlation B3LYP functional was used.[32,33] Double-zeta LANL2DZ pseudopotentials were introduced to alleviate the electronic structure calculations.[34−36]

■ RESULTS AND DISCUSSION

Particle Characterization. The Fourier transformed infrared (FT-IR) spectrum of fresh BUSiNPs (see Figure 1a) shows strong peaks due to surface absorbed TOAB[37] (2954, 2922, 2851, 1468, 1089, 753, and 723 cm^{-1}) and very small peaks at 520 and 545−580 cm^{-1} due to Si−Cl bending and Si−Cl stretching, respectively.[38] Absorption peaks at 2100−2250 cm^{-1} expected for Si−H$_x$ stretching modes are absent. The negligible absorption at 1100 cm^{-1} and the absence of peaks at 3400 cm^{-1} assigned to Si−O−Si and Si−OH vibrations,[23,39] respectively, support the absence of oxygen structures in freshly prepared particles. Two-months aging of BUSiNPs results in surface oxidation as denoted by an increase of the IR absorption at 1100 and 3400 cm^{-1} relative to the peaks at 2954 and 1468 cm^{-1} due to TOAB (see Figure 1a). For comparison, the FT-IR spectrum of TDSiNPs is also shown. These particles show the characteristic IR absorption peaks of Si−O−Si and Si−OH vibration modes.
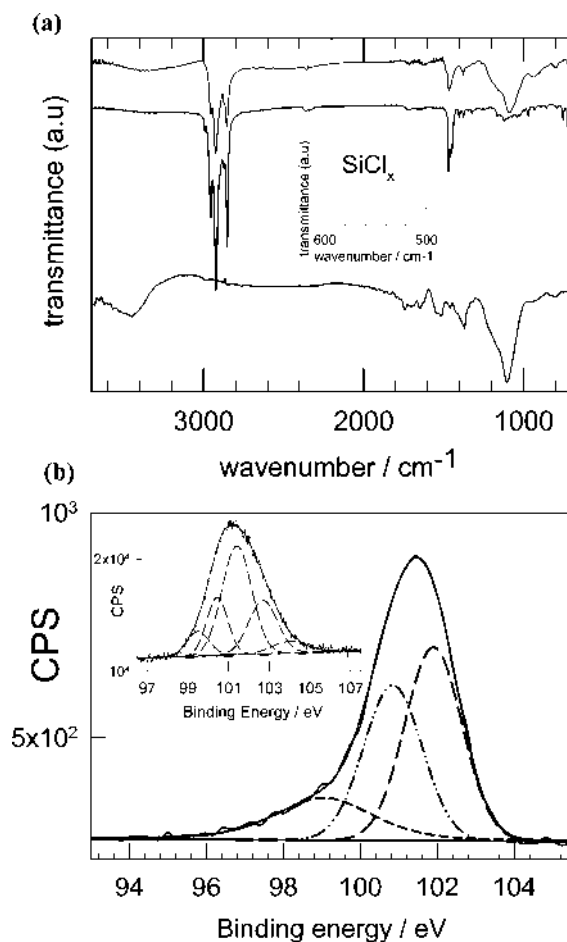

Figure 1. (a) IR of (from top down) aged and fresh BUSiNPs and TDSiNPs. Inset: Peaks due to SiCl$_x$ vibration modes of BUSiNPs. (b) Si 2p XPS peaks observed for fresh (main) and two months-aged (inset) BUSiNPs.

The XPS spectrum obtained for BUSiNP shows silicon signals strongly sensitive to particle aging (see Figure 1b). The Si 2p region of freshly prepared particles displays the contribution of silicon environments with binding energies (BE) of 99.0, 100.8, and 101.9 eV. On the other hand, two-month aged particles show silicon environments of 99.5, 100.4, 101.4, 102.7, and 103.9 eV BE. Peaks at 99.0−99.5 eV are attributed to Si−Si coordination,[40] as also supported by the Si 2s signal showing the contribution of a peak at 150.3 eV characteristic of this environment. Peaks at 100.6, 101.3, and 102.4 eV were assigned to Si$^+$, Si^{2+}, and Si^{3+} oxidized silicon, respectively, in either Si(−O−)$_x$ or Si(−Cl)$_x$ coordinated compounds with x = 1, 2, and 3 (see Supporting Information XPS Spectra). Ratios between the elements corrected signal area for the instrument sensitivity yield an average Si$_{4.5}$O$_5$Cl$_1$ surface composition for the aged particles.

Both IR and XPS data agree in indicating that the surface of freshly prepared particles is chlorinated[41] and is partially oxidized to SiO$_x$ upon aging. Surface Si−Cl oxidation to SiO$_x$ by O$_2$(g) and/or small amounts of H$_2$O is spontaneous due to their large negative change in the Gibbs free energy, in analogy to SiCl$_4$ oxidation.[42]

An average BUSiNP particle size of 1.7 ± 0.8 nm was estimated by TEM (see Supporting Information TEM), in agreement with reported sizes (1.6−1.8 nm) for SiNPs

synthesized by similar chemical wet methods involving inverse micelles.[11,13]

SAXS experiments with toluene suspensions of BUSiNP indicate the presence of a distribution of particles with different sizes/shapes as indicated by the upward curvature of the Guinier plot obtained from the scattering curves (see Figure 2a). Analysis of the region at high-q^2 values of the Guinier plot
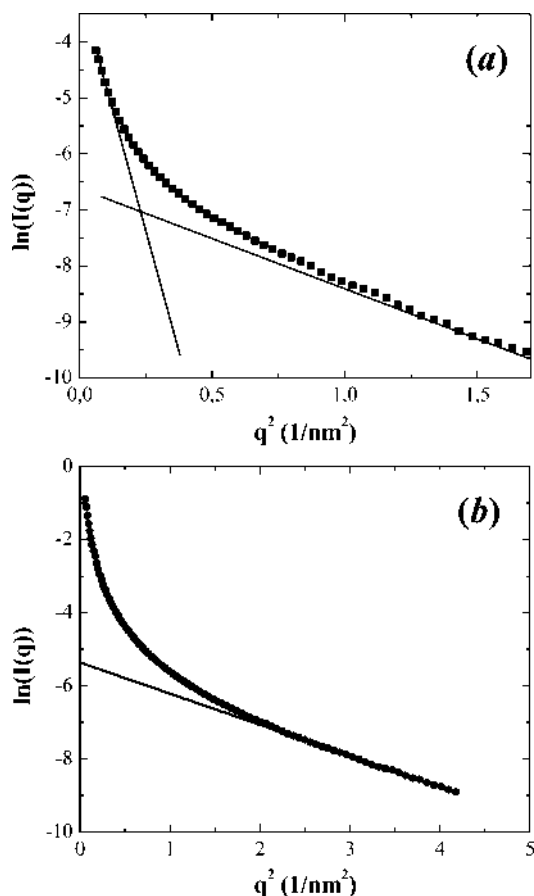

Figure 2. Guinier plot obtained from the scattering curves in SAXS experiments with toluene suspensions of (a) BUSiNP and (b) BUSiNP inside TOAB micelles.

indicates the existence of particles with gyration radii R_g = 2.4 nm, while the slope of the low-q^2 portion indicates the existence of larger structures with R_g = 6.9 nm. Clearly, sizes within both values cannot be ruled out. Although it is not easy to formulate a structural model able to totally reproduce the SAXS data, the values obtained for the highest and lowest R_g and the PDDF curve obtained from the experimental data (not shown) suggest the presence of chain-like structures in toluene suspensions.

To evaluate the influence of aggregation on the excitation–emission properties of the particles, analysis was performed with freshly synthesized particles still inside TOAB micelles (TOAB precipitation was avoided in the synthesis procedure, see Materials and Methods). Under these conditions, SAXS experiments show signals characteristic of spherical particles with R_g = 1.6 ± 0.1 nm compatible with BUSiNPs of 2 nm size surrounded by a TOAB shell. An estimated 0.7 nm TOAB thickness is also predicted from configuration calculations of TOAB's hydrocarbon chain length. However, the upward curvature of the Guinier plot in Figure 2b indicates the

presence of non-negligible amounts of bigger micelles. The presence of an approximate 2 nm size particle population inferred from these experiments is in agreement with those observed by TEM.

Photoluminiscence Experiments. Freshly synthesized BUSiNPs show structureless PL in the wavelength range from 300 to 600 nm, with emission spectra strongly depending on the excitation wavelength in the 300–500 nm range (see Figure 3 for the excitation–emission matrix). The dependence of the emission spectrum on the excitation wavelength may indicate the contribution of different emitters due to the different particle size, morphology, agglomeration, and/or oxidation grade. Therefore, the contribution of different emitters to the overall excitation–emission matrix was analyzed on the assumption that single chromophores existing in a unique form show an excitation wavelength-invariant emission spectrum (see Materials and Methods). The analysis of the matrix with the bilinear program indicates a minimum of three different emitting states or species contributing to the total emission. The emitting species show distinguishable excitation–emission spectra (see Figures 3c) and were named E1, E2, and E3 according to their excitation–emission maximum (λ_{exc}/nm, λ_{em}/nm): (340, 400), (380, 440), and (430, 510), respectively. The dispersion-corrected absorption spectra of toluene suspensions of BUSiNPs (see Figure 3b) show absorption maxima at ∼320–330 nm and 370–380 nm. The coincidence between the absorption and excitation maxima obtained for E1 and E2, and the less significant contribution of species E3 (see Figure 3b), further supports the presence of a minimum of three discernible emitting species.

The emission of Ar-saturated toluene suspensions of BUSiNPs obtained upon excitation at 340 nm yield traces that could be well fitted to a biexponential function with decay times of 1.5 and 7.8 ns with 51 and 49% contribution to the overall emission, respectively. Fitting to a stretched exponential function as expected for a disordered system with a distribution in the size and surface configuration of the nanoparticles[43] was not good. The short-lived component contributes to the emission with spectrum and % contribution coincident with those expected for E1, while the long-lived component contribution resembles the emission spectrum of E2, as shown by the triangles in Figure 3c1 and c2, respectively. Excitation at 460 nm yields an emission spectrum coincident with that of E3 showing a characteristic decay time of 2.9 ± 0.1 ns independent of the presence of O_2.

Toluene suspensions of freshly synthesized particles inside TOAB micelles show an excitation–emission matrix with reduced emission intensity. The bilinear analysis of the matrix indicates a minimum of two species showing distinguishable excitation and emission spectra which strongly resemble those of species E1 and E2 (see Supporting Information BUSiNP-TOAB). Considering that BUSiNP toluene suspensions with minimized TOAB show a significant contribution of aggregated particles, vide supra, the excitation–emission spectra of species E3 may be a consequence of particle agglomeration.

Particle aging leads to an increased PL with different excitation–emission spectrum. Further elimination of TOAB after surface oxidation does not change the excitation–emission spectrum, though it leads to an 80% additional increase in the PL intensity. For simplicity, aged particles prepared by a BU synthesis with reduced content of TOAB are referred to as BUSiNPOX. The excitation–emission matrix and the absorption spectrum of argon-saturated BUSiNPOX toluene
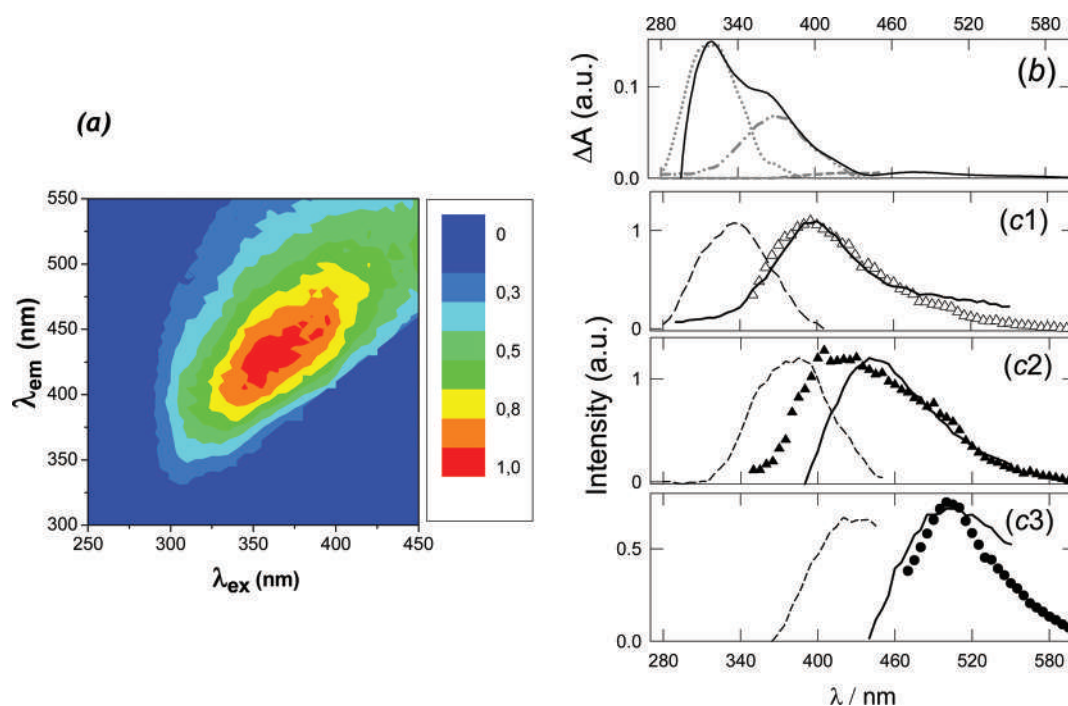
Figure 3. (a) Excitation−emission matrix of toluene suspensions of BUSiNP. (b) Corrected absorbance spectrum of an argon-saturated toluene suspension of BUSiNPs. The gray lines show the contribution to the overall absorbance due to E1 (dotted lines), E2 (dotted-dashed line), and E3 (dashed line). (c) Emission (full lines) and excitation (dashed lines) spectra of E1, E2, and E3 (graphs c1, c2, and c3, respectively) (see text). The graph scales are correlated to show the relative contribution of each emitting species to the overall emission. (Δ) and ($\blacktriangle$) stand for the contribution to the overall emission due to the transients with 1.5 and 7.8 ns decay times, respectively, observed upon 340 nm excitation. ($\bullet$) Emission spectrum of the transient observed upon 460 nm excitation.

suspensions are shown in Figures 4a and b, respectively. The luminescence quantum yields of these suspensions are Φ = 0.17.

The bilinear analysis of the excitation−emission matrix of argon-saturated toluene suspensions of BUSiNPOX shows the contribution of a minimum of three emitting species with excitation and emission maxima (λ_{exc}/nm, λ_{em}/ nm): (340, 400), (375, 435), and (300, 340), respectively, as shown in Figures 4 c1, c2, and c3. The coincidence between the absorption maxima of BUSiNPOX suspensions and the excitation spectra of these species (see gray lines in Figure 4b) further supports the presence of a minimum of three emitting species.

Because the excitation−emission spectra in Figure 4 c1 strongly resemble those of E1, it is assigned to this species.

Upon 340 nm excitation, the emission traces of BUSiNPOX suspensions may be fitted to a biexponential decay with decay times of 1.6 and 6.7 ns with 68 and 32% contribution to the overall emission, respectively. The contribution to the emission spectrum of the short-lived component resembles the emission spectrum of the species in Figure 4 c2, except for an increased emission below 400 nm which could be attributed to species E1 also showing a lifetime in the 1.5 ns range.

On the other hand, the contribution of the long-lived component does not match the emission spectrum of any of the species identified by the bilinear analysis of BUSiNPOX suspensions. However, the emission of this component (closed triangles in Figure 4 c1) strongly resembles E2 (see Figure 3 c2). It should be noted that the acquisition of the excitation−emission spectrum of the individual components from a bilinear analysis of a multicomponent system is not always possible in those cases where the emission and excitation spectra of the

different species are superimposed. A further disadvantage is a low contribution of one of the species to the overall emission. In these cases, the two components may not be differentiated by a bilinear analysis.

Species E1 and E2, showing a low contribution to the PL of the aged suspensions, suggest their presence as remaining traces of unoxidized particles. Only the species with excitation−emission spectra shown in Figures 4 c2 and c3 are due to the aging of the particles and will be denoted as E4 and E5, respectively.

TDSiNPs are composed by a silicon core and a SiO_x shell, which becomes hydroxylated in aqueous environments (Si−OH surface groups are formed).[23] The excitation−emission matrix and the corrected absorption spectrum of argon-saturated toluene suspensions of these particles are shown in Figures 5a and b, respectively. A luminescence quantum yield Φ = 0.4 is obtained for these particles. The bilinear analysis of the excitation−emission matrix of these suspensions indicates the contribution of a minimum of two species with excitation and emission maxima (λ_{exc}/nm, λ_{em}/ nm), (375, 435) and (305, 365), respectively, as shown in Figures 5 c1 and c2, respectively. Upon 340 nm excitation, the emission decay of these suspensions may be fitted to two decay times of 1.4 and 9.5 ns with 65 and 35% contribution to the overall emission, respectively. The emission spectrum of the species with 1.4 ns decay time correlates well with that in Figure 5 c1, while that with 9.5 ns correlates with the spectrum in Figure 5 c2, as shown by the symbols in the figures. The excitation spectra of the two identified species are within the broad band of the absorption spectrum (see gray lines in Figure 5b).

The coincidence observed between the peak-structured excitation−emission spectra and decay lifetimes in Figure 5
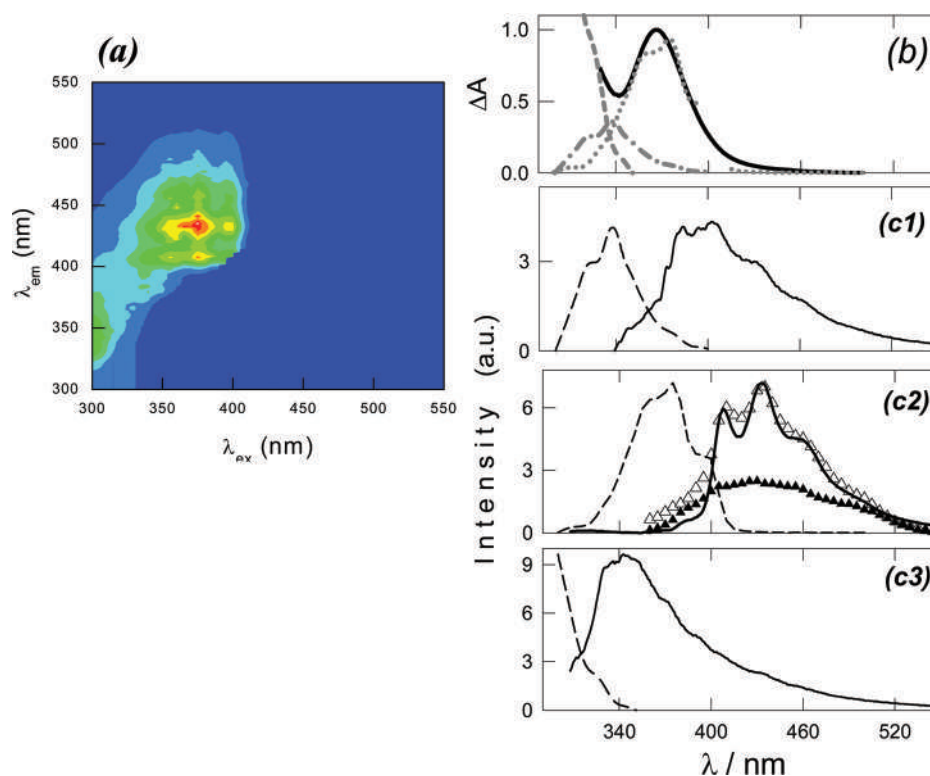
Figure 4. (a) Steady-state excitation−emission matrix of argon-saturated BUSiNPOX toluene suspensions. (b) Corrected absorbance spectrum of the same suspensions. The gray lines show the contribution to the overall absorbance of the excitation spectra shown in graphs c1 (dotted-dashed line), c2 (dotted line), and c3 (dashed line), respectively. (c) Excitation (dashed lines) and emission (solid lines) spectrum of the emitting species retrieved from the bilinear analysis (graphs c1, c2, and c3). The graphs' scales are correlated to show the relative contribution of each species to the overall emission. (Δ) and (▲) stand for the contribution to the emission spectra of the species with decay times of 1.6 and 6.7 ns, respectively, obtained upon 340 nm excitation of the suspensions.

c1 and those of E4 indicates that both PL transitions are produced between the same energy levels. Given that the transition is mainly observed in surface-oxidized particles, it is probably associated to the presence of surface SiO_x. However, because it is originated in particles of different size and oxidation extent, the emitting species in Figure 5 c1 will be denoted as E4′. TRES experiments show that the short decay component due to E4′ does not depend on the presence of dissolved O_2, in agreement with the observation that mainly E4′ contributes to the overall emission in O_2-saturated suspensions (see Supporting Information TDSiNP PL). The emitting species responsible for the excitation−emission spectra in Figure 5 c2 will be denoted as E6.

Molecular oxygen mainly depletes the long components ($\tau > 1.5$ ns) of the emission decay obtained for BUSiNP, BUSiNPOX, and TDSiNP (see Table 2) since decay times in the subnanosecond regime are insensitive to diffusion-controlled processes. Plots of $1/\tau$ vs $[O_2]$ yield a diffusion-controlled dynamic quenching rate constant $k_Q = 2 \times 10^{10}$ M^{-1} s^{-1}, thus indicating an efficient transfer of the excited state energy to O_2. On the other hand, plots of Φ^{-1} vs $[O_2]$ yield, within the experimental error, Stern−Volmer constants $K_{sv} = (63 \pm 9)$ M^{-1} for BUSiNPOX and TDSiNP (see Table 2 and Supporting Information O_2 effect on PL). Considering that Φ values show the contribution of long- and short-lived species and the latter species may only be quenched by static mechanisms,[7] K_{sv} values also rely on the O_2-adsorption capacity of the particles. These observations are of interest for potential applications of the particles as photosensitizers.[7]

Anisotropy Experiments. Time-domain anisotropy experiments were performed for BUSiNP, BUSiNPOX, and TDSiNP toluene suspensions. The measured anisotropy time profiles follow a single exponential with $r(t) = r_o \times \exp(-t/\theta)$ (see Figure 6), from which the rotational correlation times θ and the anisotropy at time zero r_o are determined. The observation of a single exponential indicates that the emission mainly originates from a population of particles with three identical perpendicular rotational axes. The time of Brownian rotation of a molecule, θ, gives information on the hydrodynamic radius (R) by the Stokes−Einstein−Debye relation.[44] On the other hand, r_o is related to the relative orientation of the excited- and fundamental state dipole moments of the particles.

The time-domain anisotropy experiments with toluene suspensions of BUSiNP were performed exciting at 340 and 460 nm to isolate E1 and E2 from E3, respectively. The values $r_o = 0.07 \pm 0.03$ and 0.04 ± 0.03 obtained for these species are coincident within the experimental error. Taking the value 554.2 μPa·s for the viscosity of toluene at 303 K,[45] the estimated average hydrodynamic diameters are $<D> = (1.4 \pm 0.2)$ nm for species E1 and E2 and $<D> = (2.3 \pm 0.1)$ nm for species E3.

Anisotropy experiments performed with argon-saturated toluene suspensions of BUSiNPOX were performed exciting with light of 340 nm and detecting the emission at 415 nm. Therefore, according to Figure 4, these experiments yield information on species E1, E2, and E4. The values $r_o = 0.06 \pm 0.03$ and $<D> = (1.6 \pm 0.1)$ nm are, within experimental error, coincident with those measured for E1 and E2 in BUSiNP
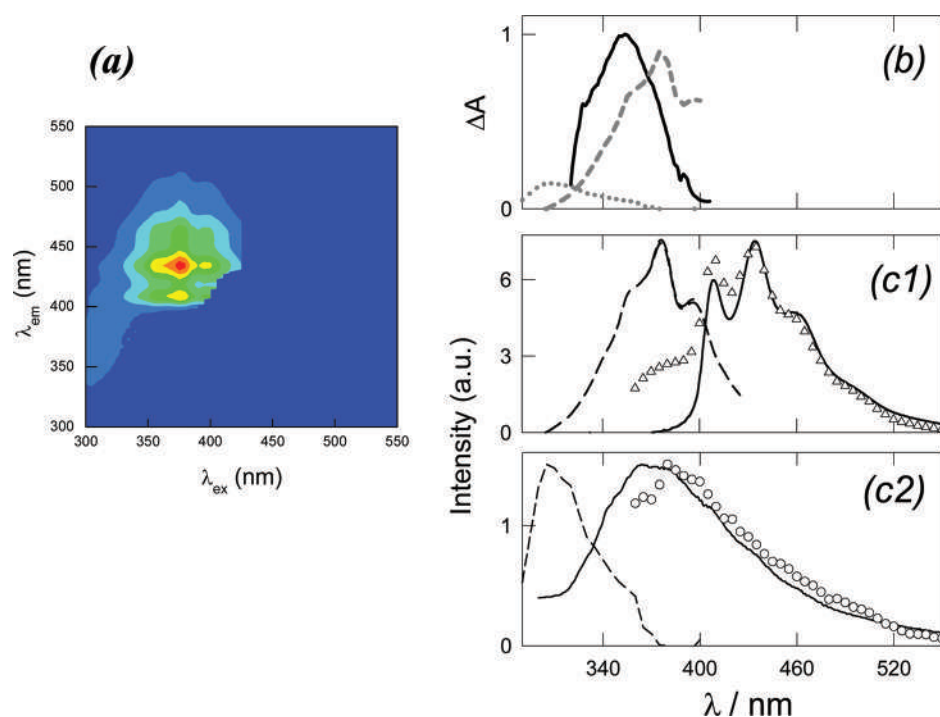
Figure 5. (a) Steady-state excitation−emission matrix of argon-saturated TDSiNP suspensions. (b) Absorbance spectrum of the same suspensions. The gray lines show the contribution to the overall absorbance of the excitation spectrum shown in graphs c1 and c2. (c) Excitation (dashed lines) and emission (solid lines) spectrum of the two emitting species retrieved from the bilinear analysis (graphs c1 and c2). The graphs' scales are correlated to show the relative contribution of each species to the overall emission. (△) and (○) stand for the contribution to the emission spectra of the species with decay times of 1.4 and 9.5 ns, respectively.

Table 2. Emission Quantum Yields (Φ), Luminescence Decay Times, and Contribution to the Total Emission, τ (%), Obtained upon 340 nm Excitation in Experiments at 298 K with Toluene Suspensions of BUSiNP, BUSiNPOX, or TDSiNP under Different O_2 Saturation

	Φ (error)			τ_{340exc}/ns (%)[a]		
[O_2]/mM	0.0	2.0	8.9	0.0	2.0	8.9
BUSiNP	--------	--------	--------	1.5 ± 0.1 (51)	--------	1.6 ± 0.1 (86)
				7.8 ± 0.3 (49)		4.6 ± 0.3 (14)
BUSiNPOX	0.17(0.03)	0.13(0.02)	0.10(0.02)	1.6 ± 0.1 (68)	1.3 ± 0.1 (68)	1.1 ± 0.1 (71)
				6.7 ± 0.3 (32)	4.9 ± 0.3 (32)	3.2 ± 0.3 (29)
TDSiNP	0.40(0.04)	0.30(0.04)	0.26(0.04)	1.4 ± 0.1 (65)	-------	1.4 ± 0.1 (93)
				9.5 ± 0.3 (35)		5.8 ± 0.3 (7)

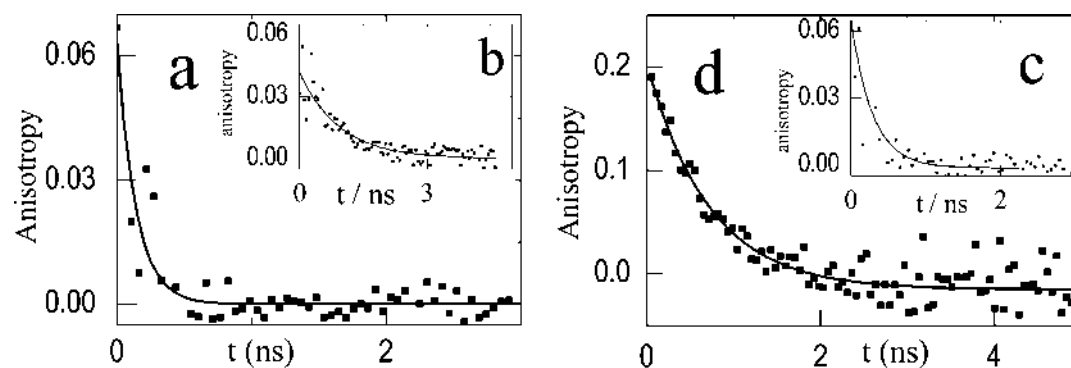[a]In all cases chi-squares range from 0.9 to 1.3.

Figure 6. Time-resolved anisotropy experiments of argon-saturated toluene suspensions of (a) BUSiNPs, 340 nm excitation and 415 nm emission detection; (b) BUSiNPs, 460 nm excitation and 500 nm emission detection; (c) BUSiNPOX, 340 nm excitation and 415 nm emission detection; and (d) TDSiNPs, 340 nm excitation and 415 nm emission detection.

suspensions, thus indicating that surface oxidation does not significantly change the particle size. Anisotropy studies including E5 could not be performed because of equipment limitations for exciting samples below 340 nm.

Anisotropy experiments performed exciting argon-saturated toluene suspensions of TDSiNPs at 340 nm, and detecting the emission at 415 nm yields information on species E6 and E4′. The obtained values $<D>$ = (2.2 ± 0.1) nm and r_o = 0.25 ± 0.02 are in agreement with previously reported values for air-saturated toluene suspensions of TDSiNPs and their surface derivatives.[23] Therefore, the dipole orientation of the excited states leading to the observed luminescence does not depend on the surface coverage with organic molecules. The value r_o = 0.25 clearly indicates a different orientation of the fundamental and excited state dipole moments, also in agreement with the large Stokes shift observed for E4′.

Theoretical Calculations. Figure 7 shows the optimized geometries for 1.2, 1.8, and 2.1 nm size SiNPs with surface Si—
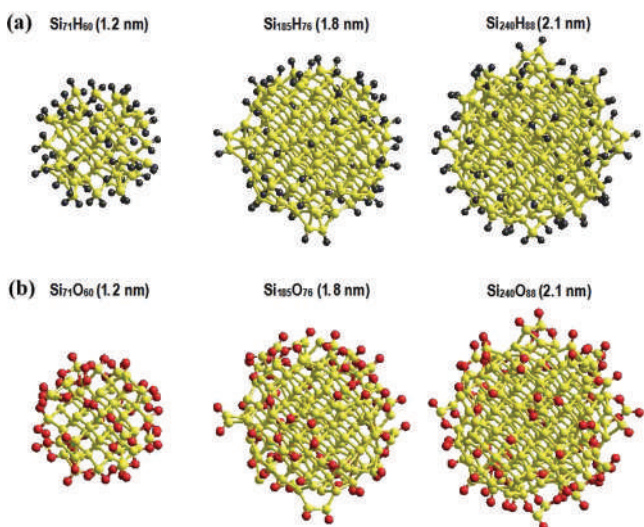

Figure 7. Optimized geometries, in vacuum at 0 K, for (a) H- and (b) O-terminated SiNPs of 1.2, 1.8, and 2.1 nm, shown in relative scales. Si, yellow; H, black; and O, red.

O and Si—H terminations. Because of the generation method, these particles resemble those obtained in a top-down procedure.

Oxidized particles were obtained,substituting all the hydrogen atoms in the stabilized particles by oxygen atoms. The energy increment (ΔE) of this process is calculated using eq 1, where n stands for the number of Si atoms and y is the number of surface bonds.

$$\Delta E = E(Si_nO_y) + y \cdot E(H) - E(Si_nH_y) - y \cdot E(O) \qquad (1)$$

The variation of ΔE with the particle diameter is shown in Supporting Information Energy increment. For all the particle sizes calculated, an increase of the particle stability upon surface oxidation is observed, in agreement with the spontaneity of the oxidation process. For particle diameters below 0.9 nm, the superficial oxidation yields a quantitative conversion of the silicon particle to SiO_x and concomitant important stabilization energy.

The particle crystalline structure was evaluated taking the mean Si—Si bond length and its standard deviation for the silicon atoms in the core and for those in the surface. For the $Si_{240}H_{88}$ particle, the mean Si—Si bond distance in the core and in the surface is 2.33 (0.03) and 2.20 (0.15) Å, respectively. On the other hand, for $Si_{240}O_{88}$, Si—Si bond distances of 2.30 (0.05) and 2.60 (0.30) Å were obtained for the core and the surface, respectively. Therefore, the appreciable increase in the mean bond length observed in surface Si—Si bonds upon oxidation indicates that a strong network disorder takes place while the core silicon atoms exhibit negligible distortion.

Band gaps of 4.9, 4.7, and 4.4 eV were obtained for $Si_{29}H_{24}$, $Si_{35}H_{18}$, and $Si_{47}H_{44}$, respectively, in agreement with published trends,[46] thus confirming an adequate calculation methodology. The lower energy transitions obtained for $Si_{29}O_{24}$, $Si_{35}O_{18}$ and $Si_{35}O_8$ surface oxidized particles are of 3.9, 3.7, and 4.0 eV, respectively. The method does not allow differentiating the transitions involved but highlights the role of surface SiO_x groups on the energy gap convergence of surface-oxidized particles. The contribution to the absorption at 3.8 eV of nonbridging oxygen hole centers and Si—O—O—Si defects, already observed in the optimized structures, may not be neglected.[20]

Energy Gap Calculation from Experimental Data and Correlation with Size. The absorption spectra of BUSiNP and BUSiNPOX exhibit features in agreement with the excitation spectra of the emitting species contributing to the overall emission spectrum. However, this was not the case for TDSiNP, where dark silicon fragments seem to play a dominating role in the process of light absorption. This fact indicates that the optical transmission spectrum may introduce big errors when it is used for the calculation of the energy gap of charge carriers in silicon nanoparticles. The required energy spectrum parameters can be roughly evaluated using the PL excitation spectrum, as earlier suggested in the literature.[47] Therefore, the mean band gap energy of the particles was calculated from the excitation spectrum threshold of each individual species (see Supporting Information Band Gap calculation). The calculated values are depicted in Table 3. For

Table 3. Emission Energy at Maximum (E_{em}^{max}), Energy Gaps, Predicted Size (D) Assuming Quantum Confinement-Controlled Emissions in Crystalline and in Amorphous SiNPs, and Measured Size of the Different Emitting Species

species	E_{em}^{max}/eV	energy gap (eV)	theoretical[a]D/nm	theoretical[b]D/nm	$<D>$/nm[b]	$<D>$/nm[c]
E1	3.1	3.1 ± 0.05	1.6	1.2	1.4 ± 0.2	
E2	2.8	2.8 ± 0.05	1.8	1.4		
E3	2.45	2.4 ± 0.1	2.2	1.7	2.3 ± 0.1	1.7 ± 0.8
E4	2.85, 3.0[d]	3.0 ± 0.05	----	------	1.6 ± 0.1	
E5	3.65	3.6 ± 0.1	1.3	1.1	N/A	
E4′	2.85, 3.0[d]	3.0 ± 0.1	------	------	2.2 ± 0.1[e]	3 ± 1[f]
E6	3.35	3.3 ± 0.05	1.5	1.15	2.2 ± 0.1	

[a]Theoretical correlations according to the work by Delley et al.[3] [b]Theoretical correlations according to the work by Park et al.[48] [c]Data obtained from anisotropy experiments. [d]Data obtained from TEM micrographs. [e]First and second emission maxima are denoted in order of luminescence intensity. [f]From published anisotropy experiments with TDSiNP air-saturated suspensions where E4 is the main emitting species.[23]

all the emitting species except E4 and E4′, there is a coincidence between the energy gap values and the emission maxima (see Table 3) suggesting that the excitation and the emission mainly originate from the same transition.

On the assumption that the observed luminescence is controlled by quantum confinement, the expected particle size for each species can be estimated from theoretical correlations of the band gap energy with size reported for crystalline[3] and amorphous[48] silicon (see Table 3), as the crystalline structure of the particles could not be univocally confirmed (see Supporting Information TEM Micrographs). For E1 and E2, both correlations predict, within the experimental error, particle sizes in agreement with those found experimentally. For the bigger E3 species, the predicted size assuming crystalline particles shows a better coincidence with the value obtained by anisotropy experiments. Under these arguments, the PL of E1, E2, and E3 may be considered to be controlled by the quantum confinement of carriers. The fwhm values of 40 nm observed for the emission and excitation bands of E1, E2, and E3 further support that these species stand for a monodisperse size and unique configuration of the SiNPs.

The peak-structured PL spectra of E4 and E4′ are attributed to the presence of oxygen on the particle surface. The interface between the core of the silicon nanoparticle and an outer shell of SiO_x may present lattice defects as well as a mismatch in the lattice spacing, as predicted by the theoretical calculations showing different Si−Si bond distances in the core and surface of the particles due to oxidation. These lattice defects may act as low energy traps for a photoexcited electron leading to a highly probable radiative relaxation. The observed Stokes shifts of ~0.47 eV between the maximum absorption and emission peaks of E4 and E4′ support such emission pathways. However, the excitation spectrum remains the same independent of the fact that the particles sustaining these transitions (BUSiNPOX and TDSiNP) show different hydrodynamic sizes. Therefore, these observations contradict an efficient transfer of the core charge carriers to SiO_2 surface states reported for SiO_2-embedded crystalline silicon clusters.[49]

Excitation of BUSiNPOX suspensions with light of higher frequency populates a new emitting state (E5) originally absent in the unoxidized BUSiNP suspensions. The fwhm, Stokes shifts, and the coincidence between the energy gap and emission maximum observed resemble those of quantum-confined systems with excitation and emission taking place from the same transitions. However, despite that the predicted sizes assuming crystalline and amorphous particles are almost coincident, they do not match the experimental hydrodynamic value (see Table 3). Particles of 1 nm size involve nearly 40 silicon atoms and may be regarded as clusters where it is unlikely to expect crystalline structures. Considering that the localization length of carriers in amorphous silicon is estimated to be about 0.6−1 nm,[15] the observed excitation−emission spectra might be related to the PL of a 1 nm size Si core of the oxidized particles. A similar argument might apply for E6.

According to the optimized structures, sizes of 1.6−1.8 nm observed for BUSiNP correspond to particles containing approximately 100 and 185 silicon atoms, respectively. Considering that a silicon core of ~1 nm remains after BUSiNP aging, it is estimated that >100 silicon atoms are involved in a disordered surface network as a consequence of oxidation. Therefore, a surface-localized transition giving rise to E4 emission is supported by the present results, as also

discussed in the literature for surface-oxidized silicon clusters.[17,49] A similar argument applies for E4′.

Many authors reported PL decays in the nanosecond regime for 1−2 nm size SiNPs,[50−52] in agreement with our observations. Fast decay rates were suggested to involve surface defects,[53] molecular-like traps, or shallow states,[50] as carriers generated in the core state are rapidly localized in the lower-energy surface states from which the particle emits.[19] Of these possibilities, the presence of radical defects may be neglected because of the absence of their characteristic EPR signals[54] in experiments performed with argon- and air-saturated toluene suspensions of the particles (results not shown). Our results are in agreement with the increasing evidence that SiNP radiative decay rates in the nanosecond regime result from allowed optical transitions as is the case of direct band gap semiconductors.[17,52,55]

Toluene suspensions of TDSiNPs and BUSiNPOX show anisotropy time zero values, r_o = 0.25 and 0.06, respectively (see Table 3). The different r_o values indicate the involvement of different electronic transitions. Values below r_o = 0.285 were reported for Si nanorods.[56] However, rotational correlation times measured for TDSiNP and BUSiNP suggest spherical shapes. Ideal spherical quantum dots are not expected to display anisotropy, but when the spherical symmetry is broken, effects like polarized light emission and faster radiative recombination may appear.[57,58] It seems plausible then that particle network disorder and geometry significantly contribute to r_o values. The observed anisotropy in SiNPs can be of great interest to enhance their applications in the fields of photonics and medicine and for the development of photochemical sensors.[59]

CONCLUSION

Silicon nanoparticles with an average diameter of 1.7 ± 0.8 nm were synthesized using inverse micelles and powerful hydride reducing agents. Freshly synthesized SiNPs showed excitation wavelength-dependent emission. The contribution of different emitting species to the overall excitation−emission matrix was analyzed and attributed to the direct e−h recombination in the silicon nanocrystals across the Γ−Γ direct gap. Silicon surface oxidation to SiO_x seems to introduce two different effects on the SiNP emission. An excitation−emission spectrum origi-nated in surface states associated to SiO_x was identified and corroborated in similar studies with oxidized top-down electrochemically synthesized SiNPs. On the other hand, blue-shifted emission−excitation spectra associated to the finite barrier effective mass model of the silicon core in embedded SiO_2 nanostructures were also identified.

Two important observations deserve further detailed study: the reversible quenching of luminescence by surface adsorbed particles (i.e., molecular oxygen and surfactant) and the shift of the luminescence to the red upon particle agglomeration. The first effect, which is a consequence of the high specific surface of the particles enhancing energy transfer processes to adsorbates, might be of importance for the use of the particles as radio- and photosensitizers in biological applications upon the selection of suitable acceptors.[7] The second effect might be a drawback when using the particles as optical sensors in media where agglomeration is favored.

11323

dx.doi.org/10.1021/jp2117938 | J. Phys. Chem. C 2012, 116, 11315−11325

ASSOCIATED CONTENT

S **Supporting Information**

Additional experimental details. This material is available free of charge via the Internet at http://pubs.acs.org.

AUTHOR INFORMATION

Corresponding Author

*E-mail: mcgonzalez.quim@gmail.com. Tel.: +54-221-4257430. Fax: +54-221-4254642.

Notes

The authors declare no competing financial interest.

ACKNOWLEDGMENTS

REFERENCES

(1) Burda, C.; Chen, X.; Narayanan, R.; El-Sayed, M. A. Chemistry and Properties of Nanocrystals of Different Shapes. *Chem. Rev.* **2005**, *105*, 1025−1102.

(2) Nirmal, M.; Brus, L. Luminescence Photophysics in Semiconductor Nanocrystals. *Acc. Chem. Res.* **1998**, *32*, 407−414.

(3) Delley, B.; Steigmeier, E. F. Size dependence of band gaps in silicon nanostructures. *Appl. Phys. Lett.* **1995**, *67*, 2370−2372.

(4) Mialhe, P.; Toufik, H.; Tahchi, M.; Toufik, N.; Tazibt, W. Silicon for optoelectronic. *J. Electron Devices* **2008**, *6*, 3.

(5) Swihart, M. T. *Nanotechnology in Biology and Medicine, Methods, Devices, and Applications*; CRC Press (T. Vo-Dinh): Boca Raton, 2007; Vol. 4.

(6) Nie, S.; Xing, Y.; Kim, G. J.; Simons, J. W. Nanotechnology Applications in Cancer. *Annu. Rev. Biomed. Eng.* **2007**, *9*, 257−288.

(7) Llansola Portolés, M. J.; David Gara, P. M.; Kotler, M. L.; Bertolotti, S.; San Roman, E.; Rodríguez, H. B.; Gonzalez, M. C. Silicon Nanoparticle Photophysics and Singlet Oxygen Generation. *Langmuir* **2010**, *26*, 10953−10960.

(8) Rogozhina, E. V.; Eckhoff, D. A.; Gratton, E.; Braun, P. V. Carboxyl functionalization of ultrasmall luminescent silicon nanoparticles through thermal hydrosilylation. *J. Mater. Chem.* **2006**, *16*, 1421−1430.

(9) Hua, F.; Erogbogbo, F.; Swihart, M. T.; Ruckenstein, E. Organically Capped Silicon Nanoparticles with Blue Photoluminescence Prepared by Hydrosilylation Followed by Oxidation. *Langmuir* **2006**, *22*, 4363−4370.

(10) Sankaran, R. M.; Holunga, D.; Flagan, R. C.; Giapis, K. P. Synthesis of Blue Luminescent Si Nanoparticles Using Atmospheric-Pressure Microdischarges. *Nano Lett.* **2005**, *5*, 537−541.

(11) Rosso-Vasic, M.; Spruijt, E.; Lagen, B. v.; Cola, L. D.; Zuilhof, H. Alkyl-Functionalized Oxide-Free Silicon Nanoparticles: Synthesis and Optical Properties. *Small* **2008**, *4*, 1835−1841.

(12) Rosso-Vasic, M.; Spruijt, E.; Lagen, B. v.; Cola, L. D.; Zuilhof, H., Alkyl-Functionalized Oxide-Free Silicon Nanoparticles: Synthesis and Optical Properties. *Small* **2009**, *5*, NA.

(13) Tilley, R. D.; Warner, J. H.; Yamamoto, K.; Matsui, I.; Fujimori, H. Micro-emulsion synthesis of monodisperse surface stabilized silicon nanocrystals. . *Chem. Commun. (Cambridge, U. K.)* **2005**, 1833−1835.

(14) Zhang, X.; Neiner, D.; Wang, S.; Louie, A. Y.; Kauzlarich, S. M. A new solution route to hydrogen-terminated silicon nanoparticles: synthesis, functionalization and water stability. *Nanotechnology* **2007**, 095601.

(15) Kanemitsu, Y. Efficient light emission from crystalline and amorphous silicon nanostructures. *J. Lumin.* **2002**, *100*, 209−217.

(16) Mitas, L.; Therrien, J.; Twesten, R.; Belomoin, G.; Nayfeh, M. H. Effect of surface reconstruction on the structural prototypes of ultrasmall ultrabright Si[sub 29] nanoparticles. *Appl. Phys. Lett.* **2001**, *78*, 1918−1920.

(17) Zhou, Z.; Brus, L.; Friesner, R. Electronic Structure and Luminescence of 1.1- and 1.4-nm Silicon Nanocrystals: Oxide Shell versus Hydrogen Passivation. *Nano Lett.* **2003**, *3*, 163−167.

(18) Shimizu-Iwayama, T. Mechanism of photoluminescence of Si nanocrystals in SiO2 fabricated by ion implantation: the role of interactions of nanocrystals and oxygen. *J. Phys.: Condens. Matter* **1999**, *11*, 6595.

(19) Kanemitsu, Y. Luminescence properties of nanometer-sized Si crystallites: Core and surface states. *Phys. Rev. B* **1994**, *49*, 16845−16848.

(20) Skuja, L. Optically active oxygen-deficiency-related centers in amorphous silicon dioxide. *J. Non-Cryst. Solids* **1998**, *239*, 16−48.

(21) Sychugov, I. Effect of substrate proximity on luminescence yield from Si nanocrystals. *Appl. Phys. Lett.* **2006**, *89*, 111124.

(22) Kanemitsu, Y. Mechanism of visible photoluminescence from oxidized silicon and germanium nanocrystallites. *Thin Solid Films* **1996**, *276*, 44−46.

(23) Llansola Portolés, M. J.; Rodriguez Nieto, F.; Soria, D. B.; Amalvy, J. I.; Peruzzo, P. J.; Mártire, D. O.; Kotler, M.; Holub, O.; Gonzalez, M. C. Photophysical Properties of Blue-Emitting Silicon Nanoparticles. *J. Phys. Chem. C* **2009**, *113*, 13694−13702.

(24) Landes, C. F.; Link, S.; Mohamed, M. B.; Nikoobakht, B.; El-Sayed, M. A. Some properties of spherical and rod-shaped semiconductor and metal nanocrystals. *Pure Appl. Chem.* **2002**, *74*, 1675−1692.

(25) Lakowicz, J. R.; Gryczynski, I.; Gryczynski, Z.; Murphy, C. J. Luminescence Spectral Properties of CdS Nanoparticles. *J. Phys. Chem. B* **1999**, *103*, 7613−7620.

(26) Hamai, S.; Hirayama, F. Actinometric determination of absolute fluorescence quantum yields. *J. Phys. Chem.* **1983**, *87*, 83−89.

(27) Svergun, D. Determination of the regularization parameter in indirect-transform methods using perceptual criteria. *J. Appl. Crystallogr.* **1992**, *25*, 495−503.

(28) Frauenheim, T.; et al. Atomistic simulations of complex materials: ground-state and excited-state properties. *J. Phys.: Condens. Matter* **2002**, *14*, 3015.

(29) Elstner, M.; Porezag, D.; Jungnickel, G.; Elsner, J.; Haugk, M.; Frauenheim, T.; Suhai, S.; Seifert, G. Self-consistent-charge density-functional tight-binding method for simulations of complex materials properties. *Phys. Rev. B* **1998**, *58*, 7260.

(30) Aradi, B.; Hourahine, B.; Frauenheim, T. DFTB+, a Sparse Matrix-Based Implementation of the DFTB Method†. *J. Phys. Chem. A* **2007**, *111*, 5678−5684.

(31) Granovsky, A. A. Firefly version 7.1.G. http://classic.chem.msu.su/gran/gamess/index.html.

(32) Becke, A. D. Density-functional thermochemistry. III. The role of exact exchange. *J. Chem. Phys.* **1993**, *98*, 5648−5652.

(33) Lee, C.; Yang, W.; Parr, R. G. Development of the Colle-Salvetti correlation-energy formula into a functional of the electron density. *Phys. Rev. B* **1988**, *37*, 785.

(34) Hay, P. J.; Wadt, W. R. Ab initio effective core potentials for molecular calculations. Potentials for K to Au including the outermost core orbitals. *J. Chem. Phys.* **1985**, *82*, 299−310.

(35) Hay, P. J.; Wadt, W. R. Ab initio effective core potentials for molecular calculations. Potentials for the transition metal atoms Sc to Hg. *J. Chem. Phys.* **1985**, *82*, 270−283.

(36) Wadt, W. R.; Hay, P. J. Ab initio effective core potentials for molecular calculations. Potentials for main group elements Na to Bi. *J. Chem. Phys.* **1985**, *82*, 284−298.

(37) Kinugasa, S.; Tanabe, K.; Tamura, T. *Spectral Database for Organic Compounds, SDBS*; National Institute of Advanced Industrial Science and Technology (AIST): Japan, 2009. Available online at: http://riodb01.ibase.aist.go.jp/sdbs/cgi-bin/cre_index.cgi?lang=eng

(38) Shirai, H.; Ito, T.; Ikeda, Y. Disorder-induced nucleation in the nanocrystalline silicon film growth from chlorinated materials by rf plasma-enhanced chemical vapor deposition. *J. Non-Cryst. Solids* 2004, *338−340*, 115−118.

(39) Ruiz, A. E.; Caregnato, P.; Arce, V. B.; Schiavoni, M. d. l. M.; Mora, V. C.; Gonzalez, M. C.; Allegretti, P. E.; Mártire, D. O. Synthesis and Characterization of Butoxylated Silica Nanoparticles. Reaction with Benzophenone Triplet States. *J. Phys. Chem. C* 2007, *111*, 7623−7628.

(40) Nemanick, E. J.; Hurley, P. T.; Webb, L. J.; Knapp, D. W.; Michalak, D. J.; Brunschwig, B. S.; Lewis, N. S. Chemical and Electrical Passivation of Single-Crystal Silicon(100) Surfaces through a Two-Step Chlorination/Alkylation Process. *J. Phys. Chem. B* 2006, *110*, 14770−14778.

(41) Zou, J.; Baldwin, R. K.; Pettigrew, K. A.; Kauzlarich, S. M. Solution Synthesis of Ultrastable Luminescent Siloxane-Coated Silicon Nanoparticles. *Nano Lett.* 2004, *4*, 1181−1186.

(42) Kajihara, K.; Hirano, M.; Skuja, L.; Hosono, H. Reactivity of SiCl and SiF groups in SiO2 glass with mobile interstitial O2 and H2O molecules. *J. Non-Cryst. Solids* 2007, *353*, 514−517.

(43) Chen, R. Apparent stretched-exponential luminescence decay in crystalline solids. *J. Lumin.* 2003, *102−103*, 510−518.

(44) Debye, P. *Polar Molecules*; The Chemical Catalogue Company: New York, 1929; p 77−108.

(45) Lide, D. R. *Handbook of Chemistry and Physics*; CRC Press. Inc.: Boca Raton, 2009.

(46) Wang, X.; Zhang, R. Q.; Niehaus, T. A.; Frauenheim, T.; Lee, S. T. Hydrogenated Silicon Nanoparticles Relaxed in Excited States. *J. Phys. Chem. C* 2007, *111*, 12588−12593.

(47) Saren, A.; Kuznetsov, S.; Pikulev, V.; Gardin, Y.; Gurtov, V. On the relationship between the optical transmission and photo-luminescence characteristics of porous silicon. *Tech. Phys. Lett.* 2001, *27*, 328−330.

(48) Park, N.-M.; Choi, C.-J.; Seong, T.-Y.; Park, S.-J. Quantum Confinement in Amorphous Silicon Quantum Dots Embedded in Silicon Nitride. *Phys. Rev. Lett.* 2001, *86*, 1355−1357.

(49) Brewer, A.; von Haeften, K. In situ passivation and blue luminescence of silicon clusters using a cluster beam/H[sub 2]O codeposition production method. *Appl. Phys. Lett.* 2009, *94*, 261102−3.

(50) Smith, A.; Yamani, Z. H.; Roberts, N.; Turner, J.; Habbal, S. R.; Granick, S.; Nayfeh, M. H. Observation of strong direct-like oscillator strength in the photoluminescence of Si nanoparticles. *Phys. Rev. B* 2005, *72*, 205307.

(51) He, G. S.; Zheng, Q.; Yong, K.-T.; Erogbogbo, F.; Swihart, M. T.; Prasad, P. N. Two- and Three-Photon Absorption and Frequency Upconverted Emission of Silicon Quantum Dots. *Nano Lett.* 2008, *8*, 2688−2692.

(52) Siekierzycka, J. R.; Rosso-Vasic, M.; Zuilhof, H.; Brouwer, A. M. Photophysics of n-Butyl-Capped Silicon Nanoparticles. *J. Phys. Chem. C* 2011, *115*, 20888−20895.

(53) Kuntermann, V.; Cimpean, C.; Brehm, G.; Sauer, G.; Kryschi, C.; Wiggers, H. Femtosecond transient absorption spectroscopy of silanized silicon quantum dots. *Phys. Rev. B* 2008, *77*, 115343.

(54) Poirier, R.; Avalos, V.; Dannefaer, S.; Schiettekatte, F.; Roorda, S.; Misra, S. K. Divacancies in proton irradiated silicon: variation of ESR signal with annealing time. *Phys. B: Condens. Matter* 2003, *340−342*, 752−755.

(55) Dhara, S.; Giri, P. Size-dependent visible absorption and fast photoluminescence decay dynamics from freestanding strained silicon nanocrystals. *Nanoscale Res. Lett.* 2011, *6*, 320.

(56) Allan, G.; Delerue, C.; Niquet, Y. M. Luminescence polarization of silicon nanocrystals. *Phys. Rev. B* 2001, *63*, 205301.

(57) Hu, J.; Li, L.-s.; Yang, W.; Manna, L.; Wang, L.-w.; Alivisatos, A. P. Linearly Polarized Emission from Colloidal Semiconductor Quantum Rods. *Science* 2001, *292*, 2060−2063.

(58) Bruhn, B.; et al. Controlled fabrication of individual silicon quantum rods yielding high intensity, polarized light emission. *Nanotechnology* 2009, *20*, 505301.

(59) Sajanlal, P. R.; Sreeprasad, T. S.; Samal, A. K.; Pradeep, T. Anisotropic nanomaterials: structure, growth, assembly, and functions. *Nano Rev.* 2011, *2*, 5883.